J. Hydrol. Hydromech., 73, 2025, 4, 378–395
https://doi.org/10.2478/johh-2025-0029

Journal of Hydrology and Hydromechanics

Interpretable Stacked Gradient-Boosting Models for Predicting the Discharge Coefficient of Elliptical Side Orifices

Nanes Hassanin Elmasry*, Mohamed Kamel Elshaarawy*

Civil Engineering Department, Faculty of Engineering, Horus University-Egypt, New Damietta 34517, Egypt.
* Corresponding author. E-mail: nhassanin@horus.edu.eg and melshaarawy@horus.edu.eg

Abstract: This study introduces a novel machine learning framework to accurately predict the discharge coefficient (C_d) of elliptical side orifices (ESOs). A cleaned experimental dataset consisting of 575 entries, refined using the Interquartile Range (IQR) method to remove outliers was employed. Five key dimensionless input variables were used to predict C_d: relative crest height (W/B), relative orifice width (a/B), relative orifice height (b/B), relative upstream height (y_1/B), and upstream Froude number (F_1). Four advanced Bayesian-optimized base models: Extreme Gradient Boosting (BO-XGB), LightGBM (BO-LGB), CatBoost (BO-CGB), and Histogram-based Gradient Boosting (BO-HGB) were integrated within a stacked ensemble architecture. A meta-learner based on Multiple Linear Regression (MLR) linearly combined these predictions to form the final Stacked Model (SM-MLR). Among the base models, the BO-CGB model achieved the best validation performance, with R^2=0.8884, RMSE=0.0100, and MARE=0.0155. The final SM-MLR model outperformed all base learners and prior models, reaching R^2=0.920, RMSE=0.0086, and MARE=0.0122. Model interpretation using Shapley Additive Explanations (SHAP) and Partial Dependence Plots (PDPs) revealed that a/B and b/B were the most influential. PDP analysis highlighted a consistently positive influence of a/B and a nonlinear but stabilizing trend for b/B. In contrast, W/B exhibited a strong negative linear effect on Cd, while y_1/B and F_1 showed more complex, nonlinear behaviors. These nonlinear and geometry-dependent relationships reinforce the fact that the hydraulic behavior of ESOs is not adequately captured by classical side-orifice theory. Accordingly, this study provides a comprehensive ML-based framework tailored to this geometry, and the analysis offers new theoretical insight into how ESO geometric ratios govern lateral outflow mechanics, addressing a key gap in hydraulic modeling of non-rectangular side orifice. To support practical application, a user-friendly graphical user interface (GUI) was developed, enabling engineers to estimate Cd in real time based on the input parameters. Overall, the proposed stacked ensemble approach significantly advances both the theoretical understanding and predictive accuracy of ESO discharge behavior, offering a robust and practical tool for modern hydraulic design.

Keywords: Bayesian optimization; Discharge; Elliptical orifice; Gradient Boosting; Machine learning; Prediction.

1 INTRODUCTION

1.1 Background and Importance of Side Orifices

Increasing pressure on water conservation and irrigation efficiency has driven the widespread use of flow-measurement and control structures in open-channel systems (Salmasi, 2021; Isleem et al., 2024; Afaridegan et al., 2025a). Among these, side orifices play a key functional role in irrigation networks, urban drainage systems, wastewater treatment facilities, and hydroelectric schemes. Positioned along the sidewalls of open channels, these structures divert part of the main-channel flow into adjacent areas for distribution, regulation, or treatment (Saadatnejadgharahassanlou et al., 2017, 2020; Gharehbaghi et al., 2023; Jamil et al., 2023; Hosny et al., 2025). Their operation naturally produces spatially varied flow (SVF), where the discharge progressively decreases along the channel due to lateral outflow (Karbasi et al., 2021). Because of these applications, accurately estimating the discharge coefficient (Cd) of side orifices is essential for water allocation, environmental monitoring, irrigation scheduling, and hydraulic infrastructure design.

1.2 Previous Hydraulic Studies on Side Orifices

Early investigations focused primarily on rectangular orifices, establishing foundational empirical formulations for Cd. Ramamurthy (1986b, 1987) related Cd to the orifice length–to–channel width ratio and the velocity ratio between the approaching flow and the orifice jet. Their equations included a reduction factor to account for non-uniform velocity profiles, achieving reasonable agreement with laboratory data.

Gill (1987) analyzed square orifices as a specific SVF case, neglecting frictional head losses, while Ojha and Subbaiah (1997) combined SVF theory with simplified Cd expressions validated through experiments.

The concept of an elementary discharge coefficient was later introduced by Swamee et al. (1993) to model incremental discharge through side sluice gates, incorporating gate opening and flow depth. Swamee et al. (2000) extended this approach to skewed gates. Experimental work by Esmailzadeh et al. (2015) and Masoud (2003) further demonstrated the significance of channel depth, approach Froude number, and gate geometry in shaping the discharge behavior and flow deflection near the orifice. More recent contributions by Hussain et al. (2010, 2011, 2014, 2016) compared rectangular and circular side orifices under free and submerged conditions. Their dimensionless formulations, primarily functions of the Froude number and

orifice-to-channel width ratio, achieved errors within ±5% and provided useful empirical tools for engineering design.

1.3 Strengths and Weaknesses of Traditional Modeling Approaches

Traditional empirical and regression-based equations have played an important role in predicting the discharge coefficient of side orifices by providing simple and computationally efficient tools derived from controlled laboratory experiments. Classical studies such as Ramamurthy (1986b, 1987), Gill (1987), and Ojha and Subbaiah (1997) established relationships based on geometric ratios, velocity characteristics, and SVF behavior, offering practical formulations that remain widely used in irrigation and drainage design. Their ease of application and minimal data requirements make them suitable for routine engineering tasks (Bos, 1989; Chanson, 2000). However, these methods are constrained by the simplifying assumptions on which they are based, including uniform approach flow, negligible energy losses, and idealized jet behaviour.

As a result, they struggle to represent the strongly nonlinear three-dimensional flow structures observed near side-orifice openings, particularly under high-Froude conditions, partial submergence, or when vortex formation and jet contraction occur (Hussain et al., 2010; Emiroglu et al., 2011b). Furthermore, most empirical formulas are geometry-specific, developed primarily for rectangular or square openings, and do not generalize well to nonstandard configurations such as semi-elliptical, circular, or curved planforms (Dursun et al., 2012; Hossein Zaji et al., 2015; Ismael et al., 2021). Their limited adaptability and sensitivity to boundary conditions often lead to reduced predictive accuracy when applied beyond their calibrated experimental domains (Azimi et al., 2019; Norouzi et al., 2020; Razmi et al., 2022). These limitations underscore the need for more flexible predictive approaches capable of capturing the complex nonlinear behavior governing side-orifice discharge.

1.4 Machine Learning Models for Discharge Coefficient Prediction

ML techniques have recently emerged as powerful alternatives to empirical models, offering the ability to learn complex, nonlinear relationships directly from data (Afaridegan et al., 2025a; Asgharzadeh-Bonab et al., 2025; Bijanvand et al., 2025). Algorithms such as Artificial Neural Networks (ANN), Adaptive Neuro-Fuzzy Inference Systems (ANFIS), and Support Vector Machines (SVM) have been widely applied to estimate Cd in hydraulic structures (Emiroglu et al., 2011a; Khoshbin et al., 2016; Parsaie et al., 2017a; Azimi et al., 2019; Jamei et al., 2021; Deng et al., 2023; Khosravinia et al., 2023).

To further enhance accuracy, hybrid and evolutionary techniques, such as ANFIS–GA, Gene Expression Programming (GEP), Multivariate Adaptive Regression Splines (MARS), Self-Adaptive Extreme Learning Machine (SAELM), and the Group Method of Data Handling (GMDH) have demonstrated strong performance in modeling discharge for rectangular or trapezoidal side orifices (Ebtehaj et al., 2015b, 2015a; Khoshbin et al., 2016; Azimi et al., 2017; Parsaie et al., 2017b; Mahmodian et al., 2019; Reza et al., 2019; Gharib et al., 2020; Zarei et al., 2020; Asadi et al., 2021).

2 RESEARCH NOVELTY AND CONTRIBUTIONS

Despite the growing use of elliptical side orifices (ESOs) in modern hydraulic applications, existing research remains limited in its use of advanced machine-learning methods, robust evaluation metrics, and model interpretability tools. Prior studies have mainly focused on simpler orifice geometries and traditional modeling techniques, leaving a clear need for a comprehensive, data-driven framework that can accurately predict the discharge coefficient while revealing the hydraulic role of key dimensionless parameters. This study addresses these limitations through the following contributions:

- To address the limited use of advanced machine-learning models for ESOs compared with other orifice geometries.
- To build a refined ESO database using outlier detection, descriptive statistics, and correlation analysis for reliable *Cd* prediction.
- To evaluate the influence of five key dimensionless parameters on *Cd* using correlation and density-based exploratory analysis.
- To develop and optimize four gradient-boosting models via Bayesian Optimization under 5-fold cross-validation.
- To assess model accuracy using comprehensive regression, reliability, and uncertainty metrics, supported by scatter plots and REC curves.
- To enhance interpretability through SHAP and PDP, identifying the dominant hydraulic drivers of *Cd*.
- To construct a stacked SM-MLR ensemble achieving improved accuracy and reduced uncertainty over individual models.
- To benchmark performance against prior ESO and non-ESO studies, demonstrating competitive or superior predictive capability.
- To deploy the final model through a user-friendly GUI for practical engineering applications.

3 MATERIALS AND METHODS

Fig. 1 shows the methodology used to estimate the discharge coefficient (C_d) of Elliptical Side Orifices using stacked gradient boosting techniques. The process begins with a dataset of 588 experimental records, incorporating input parameters such as relative crest height, relative orifice width and height, upstream water depth, and upstream Froude number, with C_d as the output. Exploratory data analysis includes statistical summaries, KDE plots, correlation heatmaps, and hexbin plots. The data is divided into training (70%), validation (15%), and testing (15%) sets. Four gradient boosting models: XGBoost, LightGBM, CatBoost, and HGBoost are trained using Bayesian Optimization for hyperparameter tuning. Predictions from the base models on the validation set serve as inputs to a stacked model based on Multiple Linear Regression (SM-MLR). The model is evaluated using both visual methods and quantitative metrics. Additionally, feature importance is analyzed using SHAP, relationships are interpreted via PDPs, and the results are compared with previous studies.

3.1 Database Collection

In this study, a database comprising of 588 experimental datasets was collected from Vatankhah and Rafeifar (2020), focusing on the influence of various geometric and hydraulic parameters on C_d of elliptical side orifices. They conducted the experiments in a horizontal rectangular channel (12 m length, 0.25 m width, and 0.5 m height) was used to perform

experiments. Two types of rectangular and triangular weirs were used to measure the flow through the orifice (Q_s) orifice and the upstream flow of the orifice (Q_u). Two different lengths of orifice (a = 15, 20 cm), three heights (b = 2, 3, 4 cm) and 2 crest heights (W = 5, 10 cm) were used. A total of 12 different geometric configurations were examined. The upstream discharge (Q_u) varied between 13.8 and 39.6 L/s, while the side orifice discharge (Q_s) ranged from 3.66 to 21.41 L/s.

The Froude number in the main channel (F_r) spanned from 0.22 to 0.77. C_d was computed using the following expression: $C_d = \frac{Q}{\pi.a.b\sqrt{2gh_c}}$ where (h_c = y_1–W–b). The studied factors affecting the elliptical side orifices are shown in Figure 2. They are (1) elliptic orifice dimension (a is horizontal semi-axis and b is vertical semi-axis); (2) orifice crest height (W, the distance between the channel bed and the orifice), (3) velocity in the main channel ($V_1 = \frac{Q}{A_1}$), (4) orifice upstream (y_1) and downstream (y_2) depths, (5) main channel width (B), (6) gravity acceleration (g), (7) water surface tension (σ), (8) water dynamic viscosity (μ), and (9) water density (ρ).

By using dimensional analysis, Eq. (1) is derived as presented below:

$$C_d = \varphi_1(a, b, W, B, y_1, V_1, g, \rho, \sigma, \mu) \quad (1)$$

Where φ_1 is the functional symbol. Using Buckingham's π theory (Hanche-Olsen, 2004), effective dimensionless parameters can be obtained as follows in Eq. (2).

$$C_d = \varphi_2\left(\frac{W}{B}, \frac{a}{B}, \frac{b}{B}, \frac{y_1}{B}, F_1 = \frac{V_1}{\sqrt{g.y_1}}, R_e = \frac{\rho.V_1.a}{\mu}, W_e = \frac{\sigma}{\rho.g.a^2}\right) \quad (2)$$

Where φ_2 is the functional symbol. Since gravity is the dominant driving force in open channel flow, the influences of viscosity and surface tension are negligible (Ramamurthy et al., 1986b; Vatankhah, 2016); therefore, the Reynolds and Weber numbers can be excluded from the governing equation. Eq. (2) is simplified as follows in Eq. (3).

$$C_d = \varphi_3\left(\frac{W}{B}, \frac{a}{B}, \frac{b}{B}, \frac{y_1}{B}, F_1 = \frac{V_1}{\sqrt{g.y_1}}\right) \quad (3)$$

Where φ_3 is the functional symbol. W/B is the relative crest height, a/B is the relative orifice width, a/B is the relative orifice height, y_1/B is the relative upstream height, and F_1 is the upstream Froude number.

3.2 Database Preprocessing

The database preprocessing stage is essential for preparing the dataset for model development (Eltarabily et al., 2025). This process involved outlier detection, statistical summarization, and correlation analysis to ensure data quality, consistency, and suitability for modeling. Outliers are identified and removed using the Interquartile Range (IQR) method (Davies and Gather, 1993), where values falling below Q1−1.5IQR or above Q3+1.5IQR were considered extreme and excluded. This procedure helped eliminate anomalous points that could negatively influence model training. Descriptive statistics are then calculated for all variables to provide insight into data distribution, variability, and potential irregularities (Dissanayake and Farris, 2014; Ding and Jia, 2023). To further understand relationships within the dataset, correlation analysis was carried out using hexbin visualizations and the Pearson correlation coefficient. Hexbin plots illustrated the density and distribution trends between the input and output variables, while the Pearson heatmap provided a clear overview of linear associations across all variable pairs. Together, these preprocessing steps ensured a clean, reliable, and well-understood dataset for subsequent modeling (Shang et al., 2025).

3.3 Base ML Models

In this study, four advanced ML models were employed using Python to predict the discharge coefficient C_d, a critical parameter in hydraulic engineering (Elshaarawy et al., 2025). These models are built upon the gradient boosting framework, which is known for its effectiveness in handling structured data, modeling non-linear relationships, and offering high predictive performance (Barzegar et al., 2021; Megahed et al., 2023; Das et al., 2024). The selected models: XGBoost, LightGBM, CatBoost, and HGBoost were implemented using well-established Python libraries. To enhance the predictive performance of these models, Bayesian Optimization (BO) was applied to tune their key hyperparameters (Armanuos and Elshaarawy, 2025). BO efficiently explores the hyperparameter space by balancing exploration and exploitation, enabling faster and more effective convergence than grid or random search methods. The optimization was conducted using 5-fold cross-validation over 30–50 iterations, resulting in tuned hybrid versions of each model (Armanuos and Elshaarawy, 2025). A comparative summary of the adopted models is provided in Table 1.

3.4 Stacked Model Development (SM-MLR)

To further improve prediction accuracy and generalizability, a stacked ensemble approach was employed using a linear meta-model (Elshaarawy 2025). The process involved training the four base learners (XGBoost, LightGBM, CatBoost, and HGBoost) independently on the training dataset. Their predictions on the validation set were then used as input features for the meta-model. The meta-model used in this study is a SM-MLR model, which learns to combine the outputs of the base models linearly. This structure allows the meta-model to leverage the strengths of each base learner and correct for individual weaknesses. The formulation of the SM-MLR model is given as follows in Eq. (4):

$$y = a_1x_1 + a_2x_2 + a_3x_3 + a_4x_4 + a_5 \quad (4)$$

Where y is the final predicted discharge coefficient; x_1, x_2, x_3, and x_4 are the predictions from BO-XGB, BO-LGB, BO-CGB, and BO-HGB, respectively; a_1, a_2, a_3, and a_4 are the regression coefficients learned by the SM-MLR model; a_5 is the intercept. Once trained, the SM-MLR model was evaluated on the independent test dataset and compared against the individual base models to assess the value of stacking. The SM-MLR approach balances complexity and interpretability, allowing the integration of diverse learning models into a transparent, linear framework.

3.5 Model Evaluation and Reliability Assessment

To comprehensively evaluate the predictive performance of the adopted models, both conventional regression metrics and uncertainty-based reliability measures are applied (Elshaarawy and Armanuos, 2025a). This dual assessment captures not only point-prediction accuracy but also model robustness, generalizability, and statistical consistency across the training,

validation, and testing subsets, an essential requirement for reliable hydraulic engineering prediction tasks. Traditional regression indicators were used to quantify the agreement between predicted and observed discharge coefficients, including the coefficient of determination (R^2), root mean squared error (RMSE), mean absolute error (MAE), root mean squared relative error (RMSRE), and mean absolute relative error (MARE). These metrics collectively assess model fit, error magnitude, and scale-independent predictive performance.

To complement these accuracy measures, several uncertainty-based and statistical validation metrics were incorporated to evaluate model stability and prediction reliability (Seyedian and Kisi, 2024). These include the slope indicators (k and k'), the origin-forced correlation coefficients (R_0^2 and $R_0'^2$), the robustness index (R_m), the deviation parameters (m and n), and the uncertainty measure (U_{95}). Derived from the model validation criteria of Golbraikh and Tropsha (2002), these metrics ensure that predictions remain unbiased, statistically sound, and aligned with the ideal one-to-one relationship. A summary of all evaluation metrics, their definitions, and acceptance criteria is presented in Table 2.

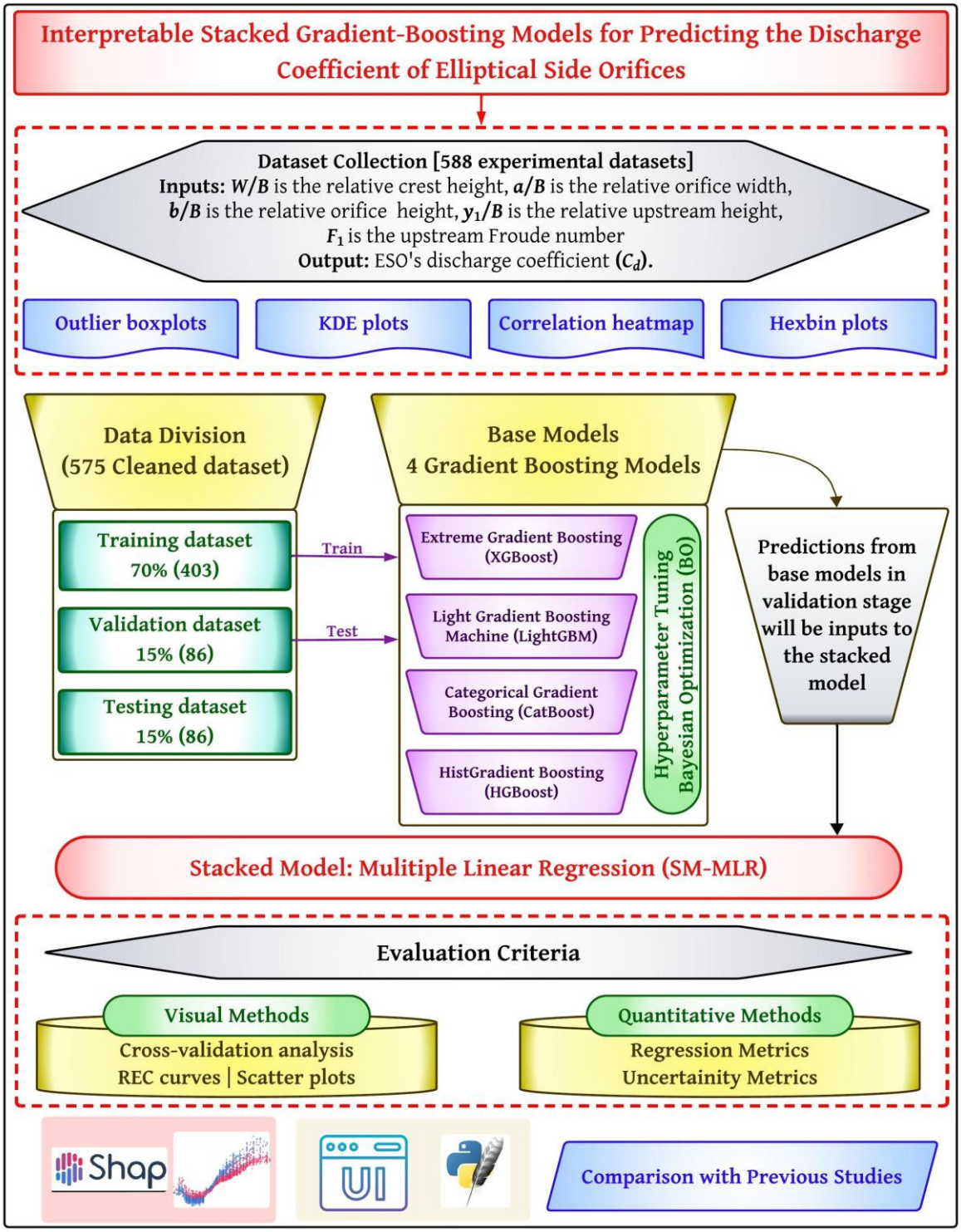

Fig. 1. Applied methodology in this study.

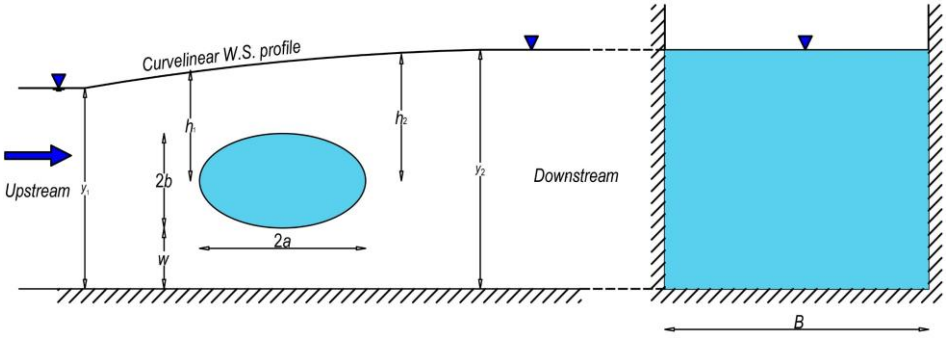

Fig. 2. Schematic representation of the elliptical side orifice, illustrating the key geometric parameters.

Table 1. Summary of the adopted gradient boosting models and the Bayesian Optimization (BO) hyperparameter ranges (Armanuos et al., 2025).

Model	Description / Key Characteristics	Advantages / Reasons for Use	Hyperparameters (BO Ranges)
XGBoost (Luat *et al.*, 2021)	High-performance boosting using second-order gradient approximation, L1/L2 regularization, and optimized tree pruning.	Strong accuracy, handles sparse data, robust with missing values.	learning_rate (0.01–0.3); max_depth (3–30); n_estimators (100–1000); subsample (0.5–1.0); colsample_bytree (0.5–1.0); min_child_weight (1–20)
LightGBM (Shen *et al.*, 2025)	Leaf-wise tree growth and histogram-based decision rules allow fast and memory-efficient learning.	High training speed, low memory usage, scalable for large datasets.	num_leaves (10–100); max_depth (−1 to 30); learning_rate (0.01–0.3); min_child_samples (5–100); n_estimators (100–1000); subsample (0.5–1.0); colsample_bytree (0.5–1.0)
CatBoost (Beskopylny *et al.*, 2022)	Native handling of categorical variables and ordered boosting to reduce target leakage.	Minimal preprocessing; strong generalization; reduces overfitting.	iterations (100–1000); depth (3–10); learning_rate (0.01–0.3); l2_leaf_reg (1–10); bagging_temperature (0–10)
HGBoost (Theerthagiri, 2025)	Fast histogram-based boosting implemented in scikit-learn, supporting efficient memory use and missing values.	Efficient on structured data; improves ensemble diversity; strong baseline learner.	max_iter (100–1000); max_depth (3–30); max_bins (50–255); max_leaf_nodes (10–200); learning_rate (0.01–0.3); min_samples_leaf (1–50); l2_regularization (1e-8–10, log-uniform)

Table 2. Summary of conventional and uncertainty-based evaluation metrics used for model performance and reliability assessment.

Type	Metric	Definition / Purpose	Interpretation / Acceptance Criteria
Regression	**R^2**	Proportion of variance in actual values explained by predictions.	Closer to 1 indicates better model fit.
	RMSE	Root mean squared difference between actual and predicted values.	Lower values indicate higher accuracy; sensitive to outliers.
	MAE	Mean absolute difference between actual and predicted values.	Lower values reflect consistent error magnitude without exaggeration.
	RMSRE	Root mean squared relative error.	Lower values indicate better scale-independent accuracy.
	MARE	Mean absolute relative error.	Lower values denote improved relative predictive performance.
Uncertainty	***k, k′***	Slope indicators comparing predicted vs. actual variability.	Acceptable range: 0.85–1.15; outside this range suggests bias.
	R_0^2, $R_0'^2$	Origin-forced correlation coefficients.	Values close to 1 indicate strong linearity through the origin.
	R_m	Combined robustness index integrating R^2 and R_0^2.	$R_m > 0.5$ indicates a robust model.
	m, n	Deviation between R^2 and origin-based coefficients.	A model is considered robust and unbiased when $\lvert m = R^2 - R_0^2 \rvert < 0.1$ and $\lvert n = R^2 - R_0'^2 \rvert < 0.1$, indicating minimal deviation from the ideal linear relationship.
	U_{95}	95% prediction uncertainty measure combining RMSE and standard deviation.	Lower values reflect stable, reliable predictions under uncertainty.

3.6 Post-Hoc Interpretation of Predictive Models

To enhance transparency in discharge coefficient prediction, this study employed two post-hoc interpretability techniques: SHapley Additive exPlanations (SHAP) and Partial Dependence Plots (PDPs) (Afaridegan et al., 2025b). SHAP, based on cooperative game theory, quantifies the contribution of each input feature to model predictions, offering both local and global interpretability. The SHAP summary and dependence plots identified key variables and illustrated their directional impact, revealing how changes in input values affect the model output. PDPs complemented SHAP by providing a global view of how individual features influence predictions, averaging out the effects of other variables. These plots helped detect non-linear trends, thresholds, and saturation effects, making them useful for engineering interpretation (Elshaarawy, 2025b).

3.7 Graphical User Interface (GUI)

A comprehensive graphical user interface (GUI) was developed to enable seamless interaction with the trained models (Elshaarawy and Armanuos, 2025b; Katlav and Ergen, 2025). The GUI allows users to input the required parameters through intuitive form fields, automatically generate predictions, and visualize key outputs such as the estimated discharge coefficient and model performance indicators. It also includes graphical displays of prediction results, enhancing interpretability and user engagement. This interface simplifies model deployment and makes the system accessible to engineers and practitioners without programming expertise (Zhang et al., 2025).

4 RESULTS

4.1 Exploratory Data Analysis

From the original 588 data points collected for C_d prediction, several outliers were identified and removed using the IQR outliers' detection method. This refinement resulted in a cleaned dataset containing 575 valid entries. Figure 3 provides an exploratory data analysis of the input and output variables used in the study, utilizing both boxplots and Kernel Density Estimation (KDE) plots to offer insights into the distribution, spread, and central tendencies of each variable. In the boxplots (Figure 3a), the variable *W/B* exhibits a narrow interquartile range (IQR) with no outliers, indicating a uniform distribution concentrated between 0.2 and 0.4. Similarly, *a/B* is tightly bounded between 0.6 and 0.8, reflecting limited variation and consistency in the relative orifice width. *b/B* shows a slightly broader spread, with its median positioned around 0.12, suggesting moderate variability in relative orifice height. For *y1/B*, the boxplot indicates a wider spread with values ranging from approximately 0.45 to just above 1.0, reflecting greater diversity in the upstream water level relative to the channel width. F_1 also exhibits a relatively wide range, with the central 50% of data distributed between approximately 0.39 and 0.58. C_d shows a symmetric distribution centered around 0.54, with minimal outliers, indicating stable and consistent output values across the dataset.

The KDE plots in Figure 3b provide deeper insight into the data by illustrating the full probability distribution of each variable beyond what the boxplots show. The distribution of *W/B* is clearly bimodal, with noticeable peaks around 0.2 and 0.4, indicating that the dataset is dominated by two primary geometric configurations. A similar pattern appears for *a/B*, which also exhibits two peaks, this time near 0.6 and 0.8, suggesting two commonly used orifice widths. In contrast, *b/B* shows a trimodal pattern, implying greater variability in the relative orifice height, likely reflecting three distinct experimental groups or design categories.

For *y1/B*, the KDE curve is moderately skewed, with the highest concentration of values near 0.7. This suggests that higher upstream depths are more frequently encountered in the dataset. The distribution of F_1 is slightly left-skewed, with most values falling between 0.4 and 0.6, indicating that subcritical flow conditions are predominant. Finally, the KDE plot for *Cd* exhibits a smooth, symmetric, bell-shaped curve centered around 0.549. This symmetry highlights the stability of the discharge coefficient and reinforces its appropriateness as the output variable for regression modeling.

4.2 Correlation analysis

The correlation heatmap (Figure 4a) displays Pearson correlation coefficients among all input parameters and *Cd*. It shows that *a/B* has the strongest positive correlation with *Cd* (0.670), indicating that increases in orifice width are generally associated with higher discharge coefficients. Similarly, moderate positive correlations are observed between *Cd* and both *b/B* (0.434) and F_1 (0.450). In contrast, *W/B* exhibits a weak negative correlation with *Cd* (–0.221), while *y1/B* shows a very weak positive correlation (0.064), indicating limited direct impact on discharge efficiency. Notably, strong interdependencies exist between some input variables, such as the high positive correlation between *W/B* and *y1/B* (0.757), and a strong negative correlation between *W/B* and F_1 (–0.719).

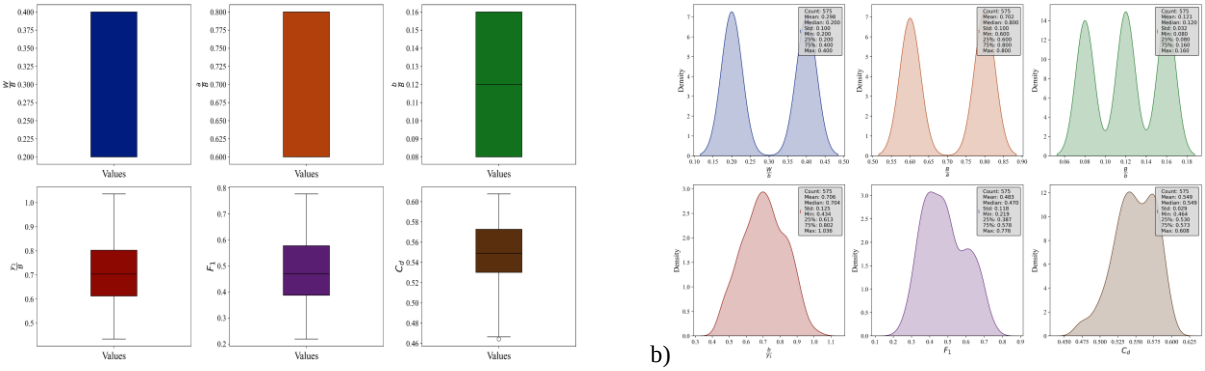

Fig. 3. Exploratory data analysis (a) Boxplots (b) KDE plots.

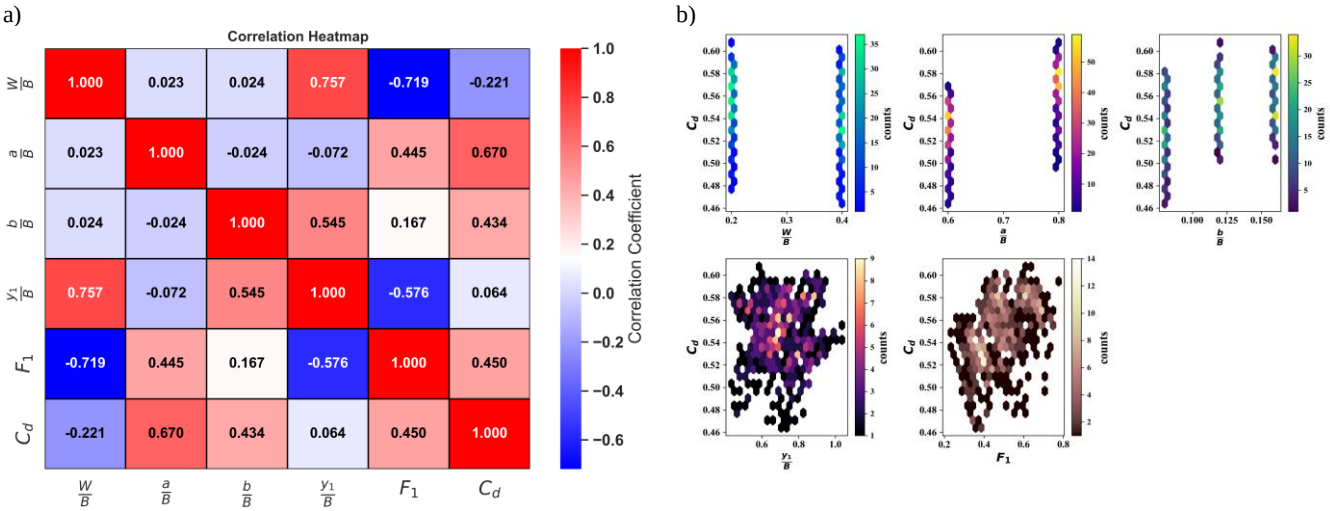

Fig. 4. Correlation analysis (a) heatmap and (b) hexbin contour plots.

Complementing the heatmap, the hexbin plots (Figure 4b) provide a visual density-based representation of the relationship between each input and C_d. The hexbin plot for *W/B* shows that the data is concentrated at two distinct vertical bands (0.2 and 0.4), which aligns with its bimodal KDE distribution and indicates two separate design scenarios. However, no strong trend between *W/B* and C_d is visually evident, supporting the weak correlation observed. In the case of *a/B*, the plot again shows two vertical concentrations at 0.6 and 0.8, with higher C_d values appearing more frequently in the upper band, reinforcing its significant positive influence. The plot for *b/B* shows three bands corresponding to discrete values, with a visible increase in C_d across higher *b/B* levels. The relationship between *y1/B* and C_d appears scattered, showing limited correlation, whereas the plot for F_1 reveals a somewhat upward trend in C_d with increasing F_1, confirming the moderate positive correlation.

4.3 Performance of Base Models

The optimized hyperparameter configurations for each base model are summarized in Table 3. These values were obtained through the BO process, aimed at minimizing prediction error during cross-validation. Each model was tuned independently to ensure optimal learning performance across its respective hyperparameter space. The selected parameters represent the most effective combinations for enhancing regression accuracy and generalization capability within the ensemble framework. Fig. 5 complements these results by visualizing the RMSE performance of the tuned models across a 5-fold cross-validation scheme. Each group of bars corresponds to fold-wise RMSE values, while the dashed line with red markers indicates the average RMSE for each model.

As shown in Figure 5, the BO-CGB model achieved the lowest average RMSE (0.0101), exhibiting both high accuracy and consistency across folds, particularly excelling in Fold 4 (0.0089). The BO-LGB model followed closely with an average RMSE of 0.0106, maintaining steady performance throughout, while the BO-HGB and BO-XGB models yielded slightly higher averages of 0.0111 and 0.0114, respectively. To further assess the stability of each model, the fold-wise RMSE values were used to compute the standard deviation (SD) and coefficient of variation (CV), where a lower CV indicates more consistent performance across folds. BO-CGB recorded a mean RMSE of 0.01014 with an SD of 0.00074 and a CV of 7.33%, confirming its strong balance between accuracy and stability. BO-HGB exhibited the lowest CV (5.58%), indicating the most uniform fold-to-fold behavior despite its higher average RMSE. In comparison, BO-XGB and BO-LGB showed slightly higher variability, with CV values of 7.55% and 8.49%, respectively.

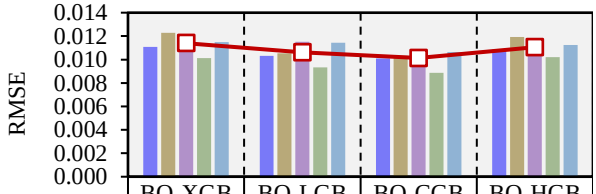

	BO-XGB	BO-LGB	BO-CGB	BO-HGB
Fold 1	0.0111	0.0103	0.0101	0.0109
Fold 2	0.0123	0.0105	0.0103	0.0119
Fold 3	0.0120	0.0115	0.0108	0.0111
Fold 4	0.0101	0.0093	0.0089	0.0102
Fold 5	0.0115	0.0114	0.0106	0.0113
Average RMSE	0.0114	0.0106	0.0101	0.0111

Fig. 5. Comparison between the base models based RMSE metric during the cross-validation process.

Together, Table 3 and Figure 5 highlight the effectiveness of BO hyperparameter tuning and the comparative strengths of the base learners. While all models performed competitively, the BO-CGB model demonstrated the best overall predictive performance, combining low average error with stable fold-wise behavior. These results reinforce its importance within the ensemble learning strategy adopted in this study.

4.3.1 Scatter plots

Figure 6 illustrates the predicted versus actual C_d for each of the base models during both training and testing phases, providing a visual evaluation of their predictive accuracy. The dashed black line represents perfect prediction (equality), while the red and green lines indicate ±10% deviation boundaries. In Figure 6a, the BO-XGB model demonstrates a high degree of fit to the equality line in the training phase with minimal spread, indicating strong learning capability. However, the validation points display a slightly broader scatter, suggesting some degree of overfitting despite an acceptable test performance with R^2 = 0.874 and RMSE = 0.011. Figure 6b shows the BO-LGB model, which maintains a tighter and more consistent alignment to the equality line across both training and testing stages. The test data follows the trend well, with a slightly improved R^2=0.887 and RMSE = 0.010 compared to the BO-XGB model, indicating better generalization and lower overfitting.

Figure 6c corresponds to the BO-CGB model, which exhibits the most concentrated clustering of points along the equality line for both datasets. The test phase accuracy is the highest among all models, with R^2=0.915 and RMSE=0.009, confirming its superior performance and consistency. The tight distribution within the ±10% bounds highlights its robustness. In Figure 6d, the BO-HGB model also shows good alignment with the equality line, achieving R^2=0.879 and RMSE=0.011 in the test phase. While slightly less precise than BO-CGB and BO-LGB, its performance remains competitive and consistent across both stages. Among all models, the BO-CGB model delivers the most accurate and stable predictions, making it the best-performing base model in this study.

Table 3. Optimized hyperparameter values for each base model after the BO process.

Model	Tuned Hyperparameters
BO-XGB	learning_rate=0.0192, max_depth=28, n_estimators=976, subsample=0.8314, colsample_bytree=0.8566, min_child_weight=12
BO-LGB	learning_rate=0.01, max_depth=30, n_estimators=1000, num_leaves=13, subsample=0.3237, colsample_bytree=1.0, min_child_samples=1
BO-CGB	learning_rate=0.01, iterations=1000, depth=6, l2_leaf_reg=1, bagging_temperature=1.7077
BO-HGB	learning_rate=0.0308, max_iter=277, max_depth=27, max_leaf_nodes=84, max_bins=255, min_samples_leaf=18, l2_regularization=5.0366×10^{-6}

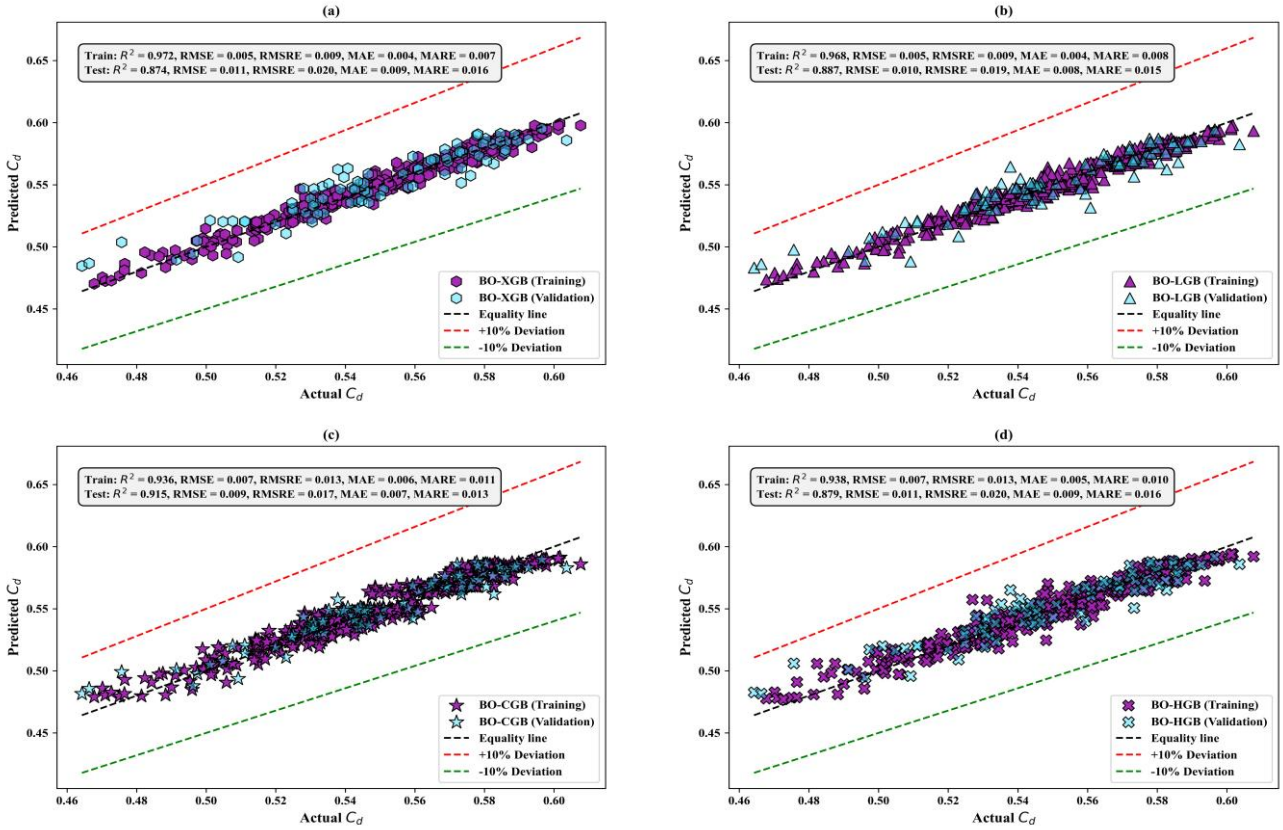

Fig. 6. Predictive performance using scatter plots across the training and validation stages of the base models (a) BO-XGB, (b) BO-LGB, (c) BO-CGB, and (d) BO-HGB.

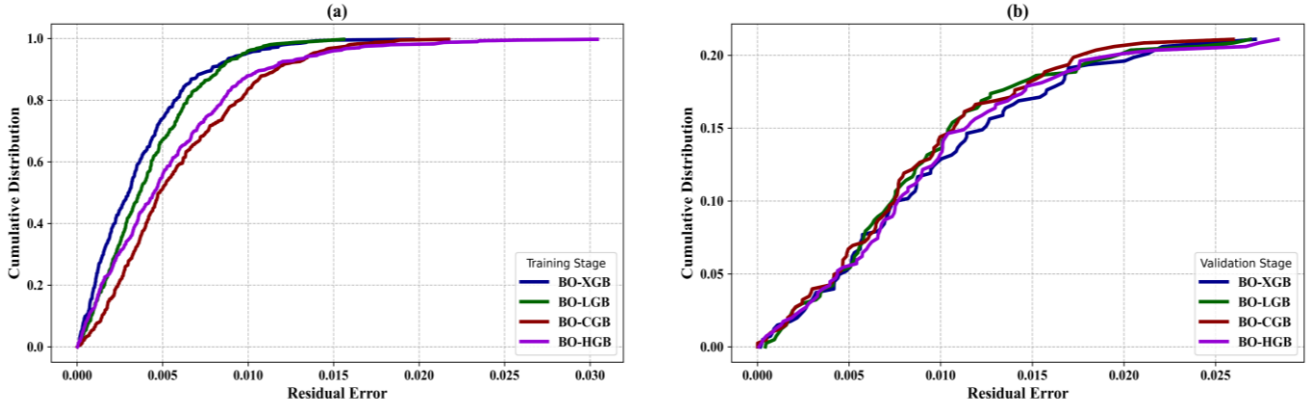

Fig. 7. Predictive performance of the base models using REC curves across the (a) training and (b) validation stages.

4.3.2 REC curves

Figure 7 illustrates the REC curves for all four base learners, providing a visual comparison of their predictive accuracy during both the training and validation phases. These curves serve as performance profiles, where a sharper incline and leftward positioning indicate superior predictive precision and faster convergence toward minimal residual error. During training (Figure 7a), the BO-XGB and BO-LGB models demonstrate the most favorable error distributions, as evidenced by their steeper gradients. Notably, the BO-XGB model achieves a marginal edge over the BO-LGB model at lower error thresholds, signifying more accurate early-stage predictions.

In contrast, the BO-CGB and BO-HGB models display flatter, more extended curves, revealing a broader error distribution and comparatively reduced precision under training conditions. During the validation stage (Figure 7b), all the four models exhibit closer performance, with their curves converging more tightly. However, the BO-CGB model maintains a slight advantage, showing a consistently higher cumulative distribution at each residual error level, particularly in the low-error region. This suggests better generalization and validation performance, aligning with previous findings. Overall, the REC curves reinforce that the BO-CGB model delivers the best balance between accuracy and stability, making it the top-performing model across both training and testing stages.

4.3.3 Regression metrics

Table 4 offers a detailed summary of the regression evaluation metrics for the four base models across both training and validation stages. The regression metrics which collectively assess the models' accuracy and predictive capability, while the uncertainty metrics provide insights into the reliability and consistency of the predictive distributions. In the training phase, the BO-XGB model achieved the highest R^2 score of 0.9722, indicating its ability to explain approximately 97.22% of the variance in the target variable, closely followed by the BO-LGB model at 0.9678. Although the BO-CGB and BO-HGB models yielded lower training R^2 scores of 0.9362 and 0.9378 respectively, they still maintained strong regression performance. This trend is mirrored in the RMSE, where the BO-XGB model recorded the lowest value (0.0047), reflecting minimal average deviation between predicted and true values. The BO-LGB, BO-HGB, and BO-CGB models followed closely with RMSEs of 0.0051, 0.0071, and 0.0072, respectively. The remaining regression indicators in training, namely RMSRE, MAE, and MARE, present similar trends. BO-XGB demonstrated the lowest RMSRE (0.0087) and MAE (0.0036), supporting its precision during training. BO-CGB showed slightly higher error values (RMSRE=0.0132, MAE=0.0059), but still within acceptable limits for practical regression tasks.

In the validation phase, the focus shifts to generalization performance. The BO-CGB model emerged as the most effective model with an R^2 of 0.8884, outperforming BO-LGB (0.8782), BO-HGB (0.8652), and BO-XGB (0.8604). This suggests BO-CGB maintained better consistency in predicting unseen data. Additionally, BO-CGB achieved the lowest RMSE of 0.0100, further confirming its superior generalization accuracy. It also showed minimal error in RMSRE (0.0186), MAE (0.0084), and MARE (0.0155), indicating robust and stable predictions across validation instances. Comparatively, the BO-XGB model exhibited the highest errors across all validation metrics, suggesting a tendency toward overfitting despite its strong training performance.

Table 4. Estimated regression metrics for the base models in the training and validation stages.

Stage	**Training**				**Validation**			
Model	**BO-XGB**	**BO-LGB**	**BO-CGB**	**BO-HGB**	**BO-XGB**	**BO-LGB**	**BO-CGB**	**BO-HGB**
R^2	0.9722	0.9678	0.9362	0.9378	0.8604	0.8782	0.8884	0.8652
RMSE	0.0047	0.0051	0.0072	0.0071	0.0111	0.0104	0.0100	0.0109
RMSRE	0.0087	0.0093	0.0132	0.0131	0.0208	0.0193	0.0186	0.0207
MAE	0.0036	0.0042	0.0059	0.0054	0.0093	0.0086	0.0084	0.0091
MARE	0.0066	0.0076	0.0108	0.0099	0.0172	0.0159	0.0155	0.0169

Table 5. Estimated uncertainty metrics for the base models in the training and validation stages.

Stage	**Training**				**Validation**			
Model	**BO-XGB**	**BO-LGB**	**BO-CGB**	**BO-HGB**	**BO-XGB**	**BO-LGB**	**BO-CGB**	**BO-HGB**
k	1.0000	1.0001	1.0001	1.0001	0.9987	0.9995	0.9981	0.9988
k'	0.9999	0.9998	0.9997	0.9998	1.0009	1.0001	1.0016	1.0008
R_0^2	0.9722	0.9678	0.9362	0.9378	0.8610	0.8783	0.8896	0.8657
$R_0'^2$	0.9703	0.9645	0.9268	0.9293	0.8322	0.8513	0.8606	0.8296
R_m	0.9538	0.9379	0.9050	0.9098	0.8457	0.8501	0.8434	0.8296
$\|m\|$	0.0004	0.0011	0.0013	0.0010	0.0004	0.0013	0.0034	0.0022
$\|n\|$	0.0024	0.0045	0.0113	0.0100	0.0338	0.0320	0.0359	0.0438
U_{95}	0.0131	0.0141	0.0198	0.0196	0.0308	0.0288	0.0275	0.0303

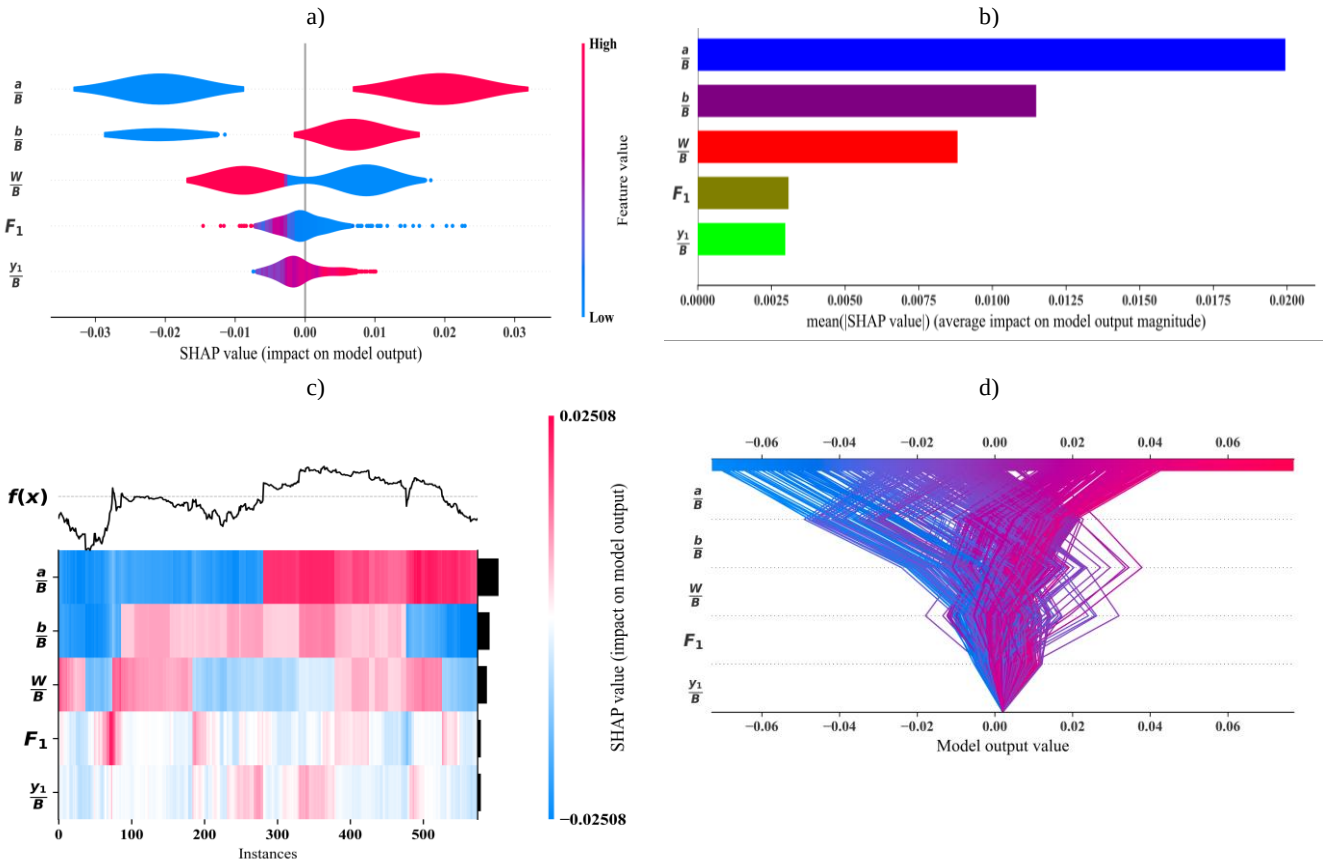

Fig. 8. Plots of SHAP analysis based on the CGB model (a) summary violin, (b) summary bar, (c) heatmap, and (d) decision river.

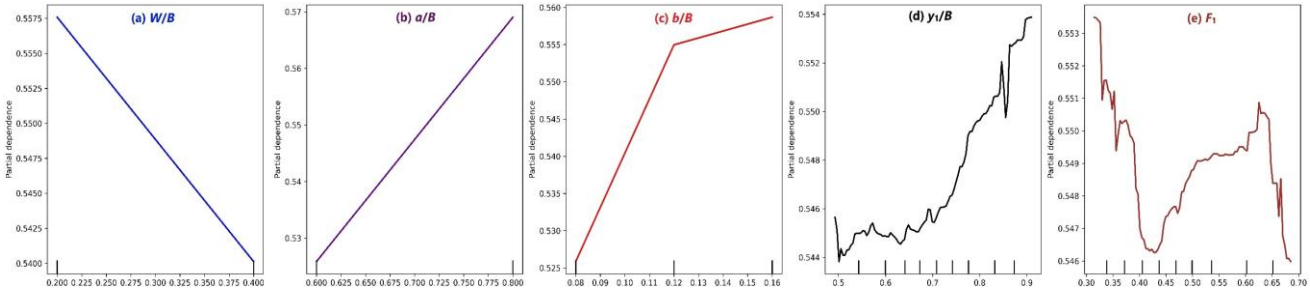

Fig. 9. Plots of PDP analysis based on the CGB model (a) W/B, (b) a/B, (c) b/B, (d) y_1/B, and (e) F_1.

4.3.4 Uncertainty metrics

Table 5 offers a detailed summary of the uncertainty evaluation metrics for the four base models across both training and validation stages. The uncertainty metrics provide another layer of evaluation. The values of k and k', which measure calibration and sharpness of predictive intervals, remained close to 1 for all models in both training and validation, indicating well-calibrated uncertainty estimates. The BO-CGB model, for instance, had k=1.0001 and k'=0.9997 in training, and maintained similar calibration in validation with k=0.9981and k'=1.0016. These results affirm that its predicted intervals were appropriately centered and spread. The coefficient of determination based on predicted uncertainty (R_0^2) and its adjusted form ($R_0'^2$) are consistent with the classic R^2 values, again highlighting model fidelity. For instance, the BO-CGB model in validation had R_0^2=0.8896 and $R_0'^2$=0.8606, aligning closely with its performance-based R^2.

Furthermore, the metric R_m, which accounts for model bias and variance, showed the BO-CGB model achieving 0.8434 in validation, slightly better than the BO-HGB and BO-XGB models, though slightly lower than BO-LGB model. Error bias ($|m|$) and dispersion ($|n|$) further revealed stability trends. The BO-CGB model had slightly higher values in validation ($|m|$=0.0034, $|n|$=0.0359) compared to training but remained within acceptable bounds. The BO-XGB model maintained the lowest validation bias at $|m|$=0.0004, but its generalization was weaker overall, as indicated by the higher RMSRE and MARE. Finally, the 95% uncertainty interval U_{95} quantifies the width of confidence bounds. The BO-CGB model had the lowest U_{95} in validation (0.0275), suggesting it not only predicted accurately but also with greater certainty and less spread in predictions. Overall, while all models exhibited competitive results, the BO-CGB model demonstrated the best balance between predictive performance and uncertainty estimation. It achieved the lowest validation RMSE, highest validation R^2, and the narrowest uncertainty bounds, establishing it as the most effective and stable model.

4.4 Model Interpretation

4.4.1 SHAP analysis

Figure 8 presents a comprehensive SHAP analysis for the BO-CGB model, highlighting the contribution of each input feature toward the prediction of C_d. The summary violin plot (Figure 8a) illustrates the distribution of SHAP values for each feature across all instances. Features like *a/B*, and *W/B* display the widest spread in SHAP values, indicating their strong and varying impact on the model's predictions. Higher values of *a/B* and *b/B* tend to increase the predicted C_d, while lower values of *W/B* are associated with decreased predictions. The summary bar chart (Figure 8b) quantifies the average magnitude of SHAP values for each input, thereby ranking the overall feature importance. According to this visualization, *a/B* exerts the highest influence on the output, followed by *b/B* and *W/B*, confirming the violin plot's implications.

The SHAP heatmap (Figure 8c) visualizes the SHAP values across individual instances for all input features. It shows localized feature impacts in detail, revealing patterns of high and low importance across specific data segments. Red hues indicate positive contributions to higher C_d predictions, while blue tones denote suppressive effects. The decision plot (Figure 8d) demonstrates how SHAP values accumulate across features for individual samples, forming the final model output. It also visually tracks the decision paths, helping understand which features consistently drive predictions higher or lower across different samples. Together, these SHAP plots confirm that geometric ratios such as *a/B* and *b/B* are the most influential in determining C_d, offering key interpretability into the BO-CGB model's decision-making process.

4.4.2 PDP analysis

Figure 9 shows the PDPs indicating the marginal effect of each input feature on the predicted output C_d as estimated by the BO-CGB model. These plots are crucial for interpreting the direction and magnitude of feature influence while accounting for potential nonlinearities and feature interactions. The feature a/B demonstrates a clear positive linear relationship with the output. As its value increases, the partial dependence on C_d steadily rises, indicating that larger a/B ratios tend to increase discharge coefficient predictions. This trend aligns with its high SHAP importance, confirming it as the most influential parameter.

For b/B, the plot shows a piecewise linear relationship, where the output increases more sharply at lower values before stabilizing. This suggests that smaller values of b/B contribute more variably to predictions, whereas its effect becomes more uniform in the upper range. In contrast, the variable W/B exhibits a strong negative linear correlation with C_d. The downward slope indicates that increasing this feature leads to a decrease in the predicted discharge coefficient, reinforcing its role as a suppressor of aerodynamic resistance within the model. The PDP for y_1/B reveals a nonlinear influence. While initially flat, the curve starts to rise at higher values, suggesting a threshold effect where y_1/B begins to contribute more positively to the discharge prediction only beyond a certain point. This delayed impact is also echoed in the SHAP analysis. Finally, the feature F_1 displays a complex, oscillating behavior, with both upward and downward trends across its range. This suggests that the model captures subtle interactions between F_1 and other features, leading to a more nuanced, context-dependent contribution to the prediction. In summary, the PDPs confirm that a/B and b/B drive C_d upward, while W/B has a suppressing effect. Among all, a/B stands out as the most dominant feature, exerting a consistently strong positive influence on the target variable.

4.4.3 Performance of the Stacked Model (SM-MLR)

To enhance prediction accuracy for the discharge coefficient (C_d), a meta-modeling strategy was implemented using a stacked ensemble framework. At the core of this approach lies the SM-MLR model, which synthesizes the predictive insights of four distinct base learners: BO-XGB, BO-LGB, BO-CGB, and BO-HGB. Rather than relying on a single model, SM-MLR integrates their outputs through a multiple linear regression mechanism, capturing the diverse learning patterns of each algorithm. This ensemble operates on the principle that combining varied predictive structures can offset individual limitations and reinforce overall reliability. By training on validation-phase predictions, the SM-MLR identifies optimal linear relationships among base model outputs, effectively assigning influence based on each model's contribution to predictive fidelity. The resulting regression expression, detailed in Eq. (5), encapsulates this synthesis and forms the foundation of the final C_d estimation.

$$C_{d(\mathrm{SM-MLR})} = -0.1549\, C_{d(\mathrm{BO-XGB})} + 0.0163\, C_{d(\mathrm{BO-LGB})} + 1.0371\, C_{d(\mathrm{BO-CGB})} + 0.1652\, C_{d(\mathrm{BO-HGB})} - 0.036 \quad (5)$$

Figure 10 presents the scatter plot of predicted versus actual C_d values using the SM-MLR model during both the validation and testing stages. The blue and pink hexagonal markers represent predictions from the validation and testing datasets, respectively. The black dashed line indicates the ideal equality line where predicted values equal actual ones, while the red and green dashed lines represent the ±10% deviation boundaries. During the validation phase, the SM-MLR model achieved an R^2 value of 0.893, indicating a strong correlation between the predicted and actual C_d values. The RMSE was 0.010, and the MAE was 0.008, demonstrating low average prediction errors. The relative error metrics were also satisfactory, with an RMSRE of 0.018 and a MARE of 0.015, affirming the model's effectiveness on the validation data. In the testing phase, the model displayed even better performance, with an R^2 value of 0.919, highlighting improved generalization capability on unseen data. The RMSE dropped slightly to 0.009, while the MAE improved to 0.007. The RMSRE and MARE also decreased to 0.016 and 0.012, respectively. These reduced error values emphasize the model's robustness and precision under testing conditions. Notably, the test predictions (pink markers) closely align with the equality line and mostly lie within the ±10% deviation band, further confirming the SM-MLR model's high accuracy, stability, and generalization power for predicting discharge coefficients in elliptical side orifices.

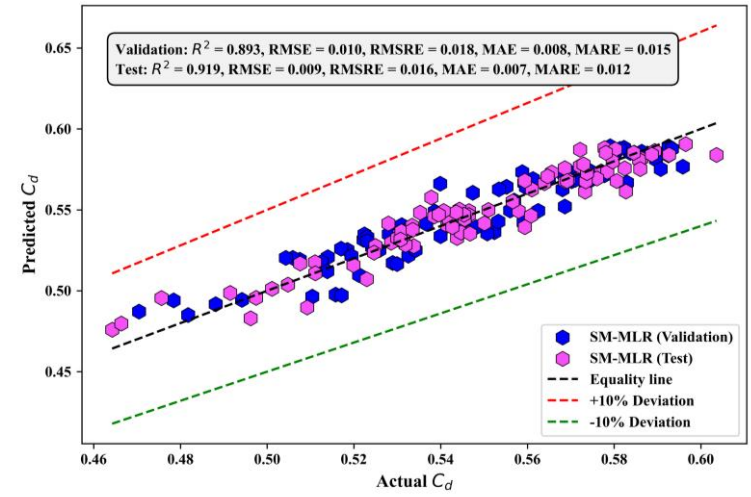

Fig. 10. Performance scatter plots of the SM-MLR model across the validation and testing stages.

Table 3. Comparison between the base models and the SM-MLR model in the testing stage using the regression and uncertainty metrics.

Metric Type	Model	BO-XGB	BO-LGB	BO-CGB	BO-HGB	SM-MLR
Regression	R^2	0.8736	0.8867	0.9148	0.8789	0.9195
	RMSE	0.0108	0.0102	0.0088	0.0105	0.0086
	RMSRE	0.0203	0.0191	0.0166	0.0199	0.0159
	MAE	0.0087	0.0080	0.0070	0.0085	0.0066
	MARE	0.0161	0.0149	0.0129	0.0159	0.0122
Uncertainty	k	0.9958	0.9981	0.9988	0.9969	1.0006
	k'	1.0038	1.0015	1.0010	1.0027	0.9992
	R_0^2	0.8794	0.8878	0.9153	0.8819	0.9196
	$R_0'^2$	0.8500	0.8559	0.8935	0.8452	0.9103
	R_m	0.8441	0.8361	0.8580	0.8257	0.9082
	$\|m\|$	0.0020	0.0044	0.0049	0.0053	0.0002
	$\|n\|$	0.0353	0.0402	0.0285	0.0468	0.0103
	U_{95}	0.0295	0.0282	0.0245	0.0290	0.0238

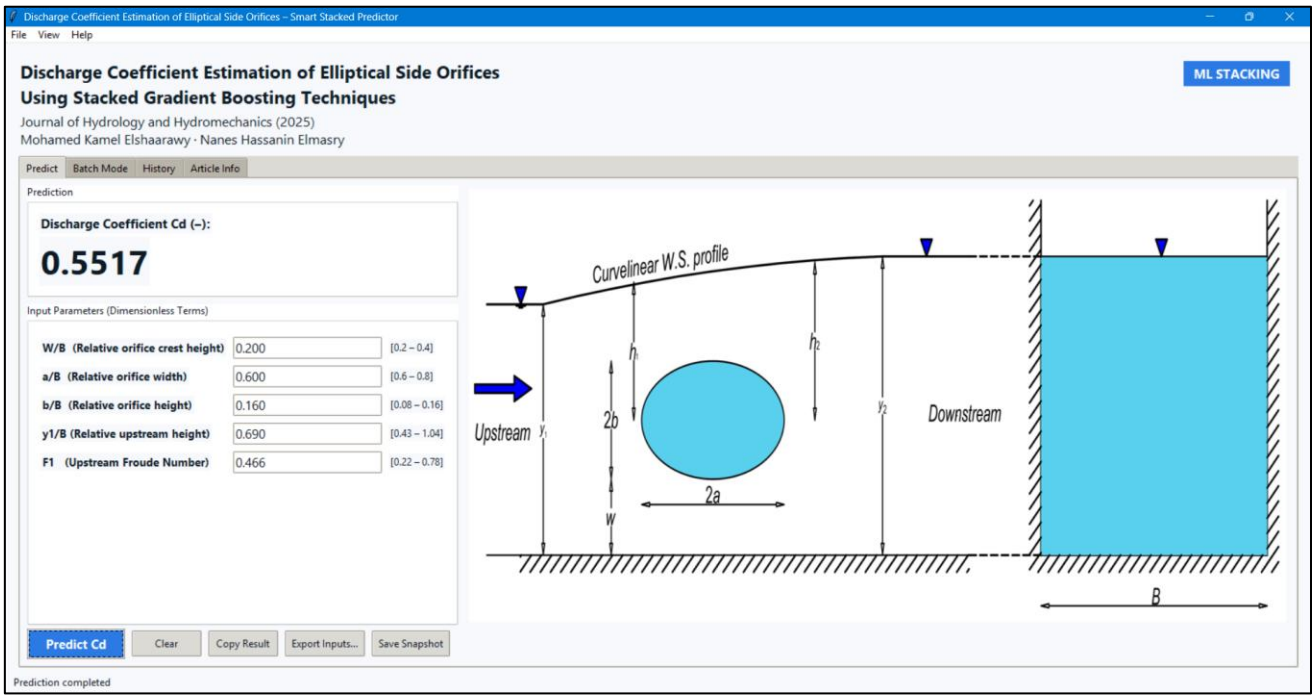

Fig. 11. Screenshot of the developed GUI to estimate C_d of ESO.

4.5.1 Comparison against the base models

Table 3 provides a comparative analysis of regression accuracy and uncertainty quantification metrics for the four base models and the SM-MLR model during the testing phase. The SM-MLR model demonstrates superior performance across nearly all evaluated criteria, highlighting the benefits of stacking in regression-based predictive modeling. From a regression perspective, the SM-MLR model achieved the highest coefficient of determination (R^2=0.9195), outperforming the strongest base learner, BO-CGB (R^2=0.9148). The root mean square error (RMSE) for SM-MLR was also the lowest at 0.0086, indicating improved precision in predicting discharge coefficients. Similarly, RMSRE and MAE values were minimized in the SM-MLR model at 0.0159 and 0.0066, respectively, demonstrating both reduced relative error and mean absolute deviation. The MARE of 0.0122 further confirms this enhanced predictive consistency, particularly when compared to the BO-XGB model (0.0161) and the BO-HGB model (0.0159). In terms of uncertainty metrics, the SM-MLR model also shows balanced and reliable results. The k and k' metrics were closest to 1 (1.0006 and 0.9992, respectively), suggesting nearly perfect proportionality and bias-free predictions. Moreover, the model had the highest R_0^2 and $R_{0'}^2$ values (0.9196 and 0.9103), emphasizing its strong alignment between predicted and observed outputs. The Rm value for SM-MLR reached 0.9082, surpassing all base models and indicating improved model reliability and applicability. Furthermore, the $|m|$ and $|n|$ values were notably minimized in the SM-MLR model (0.0002 and 0.0103, respectively). These results reflect a near-ideal agreement between predicted and actual values with reduced bias. Finally, the U_{95} metric, which measures the 95% uncertainty interval width, was the smallest for SM-MLR at 0.0238, suggesting the model delivers not only accurate but also highly confident predictions. In summary, the SM-MLR model outperformed each of the four base learners across nearly all metrics. This confirms that combining diverse gradient boosting models via linear stacking significantly improves predictive accuracy and reliability in estimating discharge coefficients for elliptical side orifices.

4.5.2 Comparison against previous studies

Based on the comparative analysis of Table 4, the current study demonstrates a notable improvement over previous efforts in predicting the discharge coefficient of elliptical side orifices. Vatankhah & Rafeifar (2020) employed a Multiple Nonlinear Regression (MNLR) model and achieved an R^2 of 0.861, with corresponding RMSE and MARE values of 0.0106 and 0.0168, respectively. Later, Karbasi et al. (2021) introduced more advanced machine learning techniques, specifically Gaussian Process Regression (GPR), which enhanced predictive accuracy, yielding an R^2 of 0.917, RMSE of 0.0081, and MARE of 0.0132. It is worth noting that Karbasi et al. (2021) partitioned their dataset using a 75% training and 25% testing split.

In comparison, the current study adopted a 70/30% data split and explored both optimized individual ensemble learners and a stacked meta-learning approach. The best-performing base model (BO-CGB) recorded an R^2 of 0.915 and an RMSE of 0.0088, closely matching the GPR model from Karbasi et al. (2021). However, the proposed SM-MLR model surpassed all, achieving the highest R^2 of 0.920, lowest RMSE of 0.0086, and a MARE of 0.0122. These results indicate that the ensemble stacking technique not only maintains strong generalization but also outperforms prior machine learning and statistical modeling efforts in terms of overall accuracy and consistency.

4.6 Model Deployment

Figure 11 illustrates the GUI developed for the proposed predictive model. This user-friendly application was designed to allow engineers and practitioners to conveniently estimate the discharge coefficient (C_d) using five dimensionless hydraulic and geometric input parameters. Upon entering these values, users can click the "Predict" button, triggering the SM-MLR to calculate the corresponding discharge coefficient. The result is displayed instantly in the output section. In the example shown, with inputs such as W/B=0.20, a/B=0.60, b/B=0.16, y_1/B=0.69, and F_1=0.466, the predicted discharge coefficient is 0.5517. This GUI reflects the practical application of the proposed machine learning framework, bridging the gap between advanced modeling techniques and real-world hydraulic engineering needs. It can be freely accessed at https://github.com/mkamel24/ESO.

5 DISCUSSION

5.1 Hydraulic interpretation of the controlling dimensionless parameters

Feature-importance and SHAP analyses identified the relative orifice length (a/B) and height (b/B) as the most influential predictors of C_d, followed by the relative crest height (W/B) as a strong negative contributor and the upstream Froude number as a secondary but nonlinearly acting variable. This structure agrees with the analytical and experimental framework developed for elliptical side orifices by Vatankhah and Rafeifar (2020).

The positive contribution of a/B and b/B to C_d reflects geometric control of the effective discharge area and vena-contracta development. Larger a/B increases the lateral extent of the opening, allowing a greater portion of the high-momentum core flow to be captured along the elliptical edge, which reduces local head losses and enhances discharge efficiency. Larger b/B deepens the jet and reduces the ratio W/B, effects that encourage a more stable and fuller contraction region. These trends are consistent with the nonlinear regression models for elliptical side orifices in Vatankhah and Rafeifar (2020) and with the kernel-based formulations of Karbasi et al. (2021), which also emphasized the sensitivity of C_d to geometric ratios.

The monotonic negative effect of W/B in the SHAP and PDP plots mirrors the role of the crest elevation in classical side-orifice hydraulics. An increased crest height reduces the effective driving head above the orifice centroid and promotes weaker lateral jets, leading to lower C_d. Similar behaviour has been documented for rectangular and circular side orifices, where the crest height or gate opening strongly influences the discharge coefficient (Hussain *et al.*, 2010, 2011).

The moderate but clearly nonlinear influence of F_1 obtained from the ML models is hydraulically consistent with the subcritical range of the original experiments ($0.22 \leq F_1 \leq 0.77$). Within this regime, geometric parameters dominate the variability of C_d, and changes in approach velocity are partly embedded in the head distribution and geometric ratios. Similar conclusions were reported for elliptical side orifices by Vatankhah and Rafeifar (2020) and for non-elliptical geometries by Hussain et al. (2010, 2011) and Ebtehaj et al. (2015a). The ML-derived importance ranking therefore aligns with established hydraulic understanding rather than contradicting it.

5.2 Consistency with analytical and data-driven models for elliptical side orifices

Performance metrics in Table 2 and Table 3 indicate that the BO-CGB and the SM-MLR models provide the most accurate predictions of C_d. For the testing stage, the BO-CGB model achieved R^2=0.9148, RMSE=0.0088, and MARE=0.0129, while the SM-MLR ensemble slightly improved these values to R^2=0.9195, RMSE=0.0086, and MARE=0.0122. These results demonstrate a reduction in both absolute and relative errors compared with the nonlinear regression equations of Vatankhah and Rafeifar (2020), which reported average relative errors between approximately 1.74% and 2.43% depending on the inclusion of F_1.

The kernel-based data-intelligence models developed by Karbasi et al. (2021) for the same ESO dataset achieved RMSE values in the range of about 0.0081–0.0085 and coefficients of determination R^2 up to approximately 0.958 for the best GPR configuration. The BO-CGB base learner in the current framework shows testing RMSE= 0.0088 and R^2=0.9148, close to the mid-range performance of the GPR ensemble, while the stacked SM-MLR meta-model slightly improves error statistics for the test set. These comparisons indicate that the inferred relationship between the input variables and the C_d is consistent with the best-performing data-driven models for elliptical side orifices and lies within a comparable accuracy range.

The distribution of residuals and the uncertainty statistics further support this consistency. For the testing data, the SM-MLR model exhibits the highest robustness index (R_m=0.9082, the largest origin-forced coefficients R_0^2 and $R_0'^2$, and the narrowest 95% uncertainty interval U_{95}=0.0238 among all learners in Table 3. These values satisfy widely accepted external-predictivity criteria used in regression modelling and indicate that the stacked model adheres closely to the one-to-one line across the range of measured C_d. Similar levels of predictive reliability were reported in the kernel-based ESO models of Karbasi et al. (2021), reinforcing the interpretation that the stacked gradient-boosting framework reproduces, rather than contradicts, existing high-quality ESO estimators.

5.3 Comparison with ensemble modelling for non-elliptical side orifices

Recent ensemble ML studies on circular and rectangular side orifices provide an additional benchmark for the performance and structure of the stacked ESO model. Deng et al. (2023) developed a hybrid ensemble based on BO-XGB and reported testing R^2 values of 0.9497 and 0.9519 for circular and rectangular side orifices, respectively, with RMSE between 0.0029 and 0.0070. The study concluded that the BO-XGB model provided the best overall compromise between accuracy and uncertainty among several ML algorithms.

The stacked SM-MLR ensemble in the present framework produces testing R^2=0.9195 and RMSE=0.0086 for elliptical side orifices, values slightly lower in R^2 and slightly higher in RMSE than those reported by Deng et al. (2023) for circular and rectangular geometries. This discrepancy is expected because the ESO dataset spans a broad range of aspect ratios and crest heights, and elliptical openings exhibit more complex geometric interactions than circular or rectangular orifices. However, the magnitude of the errors remains within the same order as those reported in Deng et al. (2023) and other ML studies on non-elliptical side orifices (Ebtehaj et al., 2015a; Azimi et al., 2021), indicating that the stacked approach yields performance comparable to state-of-the-art ensemble models across different geometries.

The structure of the optimal input set also matches conclusions drawn from non-elliptical studies. Deng et al. (2023) identified the combination of channel-width ratio, crest-height ratio, relative depth, and Froude number as the most informative predictors of C_d, an input structure analogous to the (W/B, a/B, b/B, y_1/B, F_1) set adopted here. Similar importance patterns have been reported for rectangular orifices and triangular orifices in data-driven frameworks (Vatankhah and Mirnia, 2018; Jamei et al., 2020; Moghadam et al., 2022; Khosravinia et al., 2023; Elshaarawy and Hamed, 2024). Agreement between these independent studies supports the generality of the selected dimensionless groups and the validity of the ensemble architecture.

6 CONCLUSION

This study demonstrated that predicting the discharge coefficient (C_d) for elliptical side orifices involves complex, nonlinear interactions among geometric and hydraulic variables. Traditional regression methods often fail to capture these dynamics accurately. To address this, a hybrid ensemble-learning framework was proposed using a Stacked Multiple Linear Regression (SM-MLR) approach. This model integrates four Bayesian-optimized gradient boosting algorithms (BO-XGB, BO-LGB, BO-CGB, and BO-HGB), resulting in a robust, interpretable, and computationally efficient predictive tool. Based on the findings, the following key conclusions can be drawn:

- The hydraulic behavior revealed by the ML models was fully consistent with established side-orifice theory: a/B and b/B increase C_d by enhancing jet development and effective discharge area, whereas W/B reduces C_d through its control of the available driving head. The moderate but nonlinear effect of F_1 also matched its expected influence within the subcritical flow range.
- Exploratory analysis, supported by SHAP and PDP interpretations, identified a/B (relative orifice width) and b/B (relative orifice height) as the most influential variables affecting C_d. These features demonstrated clear, consistent trends in both global and marginal analyses.
- Among the individual learners, the BO-CGB model achieved the highest performance (R^2=0.915), validating its strong ability to capture nonlinear interactions between features and C_d.
- The SM-MLR stacked ensemble model outperformed all standalone models and traditional methods, achieving R^2=0.920, RMSE=0.0086, and MARE=0.0122 on testing data. It also produced well-calibrated uncertainty metrics (coverage factor $k \approx 1$), confirming stable and reliable prediction intervals.
- The stacked framework demonstrated high external predictivity, showing strong agreement with the one-to-one line and narrow uncertainty bands, indicating that the model maintains stability across the full range of experimental C_d values.
- The SM-MLR meta-learner, based on a lightweight linear regression model, ensured fast inference while effectively combining the strengths of the base models. The ensemble

approach reduced prediction error and improved generalization, even under a more balanced 70/30 data split compared to prior studies.

- Comparison with analytical, regression-based, and kernel-based ESO models from previous studies confirmed that the proposed ensemble framework reproduces established hydraulic trends rather than contradicting them, demonstrating compatibility with both theory and prior data-driven formulations.
- A graphical user interface (GUI) was developed to allow real-time C_d estimation using five dimensionless inputs. This tool bridges the gap between advanced machine learning techniques and practical hydraulic engineering applications.

Despite the model's strong performance, its predictions are currently limited to the range of the training dataset, which primarily covers subcritical flow conditions. Expanding the dataset to include supercritical and transitional flow regimes, as well as irregular orifice geometries, would further enhance model generalization. Future research should also explore deep ensemble learning, hybrid physics-informed ML models, and integration with real-time sensor data for deployment in live hydraulic systems. Additionally, incorporating uncertainty-aware decision-making frameworks can help optimize risk assessment in practical water infrastructure applications.

REFERENCES

Afaridegan, E., Amanian, N., Goodarzi, M.R., 2025a. Hybrid Machine Learning Models for Discharge Coefficient Prediction in Hydrofoil-Crested Stepped Spillways. Archives of Computational Methods in Engineering 32 (7): 4413–4445 DOI: 10.1007/s11831-025-10274-z

Afaridegan, E., Fatahi-Alkouhi, R., Khalilian, S., Moradi-Eshgafti, A., Amanian, N., 2025b. Enhanced energy dissipation prediction in modified semi-cylindrical weirs using machine learning techniques. Modeling Earth Systems and Environment 11 (2): 131 DOI: 10.1007/s40808-025-02317-y

Armanuos, A.M., Elshaarawy, M.K., 2025. Estimating saltwater wedge length in sloping coastal aquifers using explainable machine learning models. Earth Science Informatics 18 (2): 405 DOI: 10.1007/s12145-025-01900-2

Armanuos, A.M., Zeleňáková, M., Elshaarawy, M.K., 2025. Explainable ML modeling of saltwater intrusion control with underground barriers in coastal sloping aquifers. Scientific Reports 15 (1): 29281 DOI: 10.1038/s41598-025-12830-w

Asadi, M.J., Shabanlou, S., Najarchi, M., Najafizadeh, M.M., 2021. A Hybrid Intelligent Model and Computational Fluid Dynamics to Simulate Discharge Coefficient of Circular Side Orifices. Iranian Journal of Science and Technology, Transactions of Civil Engineering 45 (2): 985–1010 DOI: 10.1007/s40996-020-00390-0

Asgharzadeh-Bonab, A., Bijanvand, S., Parsaie, A., Afaridegan, E., 2025. Machine learning-based estimation of discharge coefficient for semicircular labyrinth weirs. Scientific Reports 15 (1): 33002 DOI: 10.1038/s41598-025-18230-4

Azimi, H., Bonakdari, H., Ebtehaj, I., 2019. Design of radial basis function-based support vector regression in predicting the discharge coefficient of a side weir in a trapezoidal channel. Applied Water Science 9: 1–12 DOI:10.1007/s13201-019-0961-5

Azimi, H., Bonakdari, H., Ebtehaj, I., 2021. Gene expression programming-based approach for predicting the roller length of a hydraulic jump on a rough bed. ISH Journal of Hydraulic Engineering 27 (sup1): 77–87 DOI: 10.1080/09715010.2019.1579058

Azimi, H., Shabanlou, S., Ebtehaj, I., Bonakdari, H., Kardar, S., 2017. Combination of Computational Fluid Dynamics, Adaptive Neuro-Fuzzy Inference System, and Genetic Algorithm for Predicting Discharge Coefficient of Rectangular Side Orifices. Journal of Irrigation and Drainage Engineering 143 (7): 4017015 DOI: 10.1061/(ASCE)IR.1943-4774.0001190

Barzegar, R., Razzagh, S., Quilty, J., Adamowski, J., Kheyrollah Pour, H., Booij, M.J., 2021. Improving GALDIT-based groundwater vulnerability predictive mapping using coupled resampling algorithms and machine learning models. Journal of Hydrology 598 (February): 126370 DOI: 10.1016/j.jhydrol.2021.126370

Beskopylny, A.N., Stel'makh, S.A., Shcherban', E.M., Mailyan, L.R., Meskhi, B., Razveeva, I., Chernil'nik, A., Beskopylny, N., 2022. Concrete Strength Prediction Using Machine Learning Methods CatBoost, k-Nearest Neighbors, Support Vector Regression. Applied Sciences 12 (21): 10864 DOI: 10.3390/app122110864

Bijanvand, S., Asgharzadeh-Bonab, A., Parsaie, A., Afaridegan, E., 2025. Enhanced prediction of discharge coefficients in Harmonic Plan Circular Weirs using advanced machine learning and ensemble techniques. Flow Measurement and Instrumentation 102: 102812 DOI: https://doi.org/10.1016/j.flowmeasinst.2025.102812

Bos, M.G., 1989. Discharge measurement structures.

Chanson, H., 2000, December. A review of accidents and failures of stepped spillways and weirs. In Proceedings of the Institution of Civil Engineers-Water and Maritime Engineering (Vol. 142, No. 4, pp. 177-188). Thomas Telford Ltd. doi: https://doi.org/10.1680/wame.2000.142.4.177.

Das, P., Kashem, A., Hasan, I., Islam, M., 2024. A comparative study of machine learning models for construction costs prediction with natural gradient boosting algorithm and SHAP analysis. Asian Journal of Civil Engineering 25 (4): 3301–3316 DOI: 10.1007/s42107-023-00980-z

Davies, L. and Gather, U., 1993. The identification of multiple outliers. Journal of the American Statistical Association, 88(423), pp.782-792. https://doi.org/10.1080/01621459.1993.10476339

Deng, Y., Zhang, D., Zhang, D., Wu, J., Liu, Y., 2023. A hybrid ensemble machine learning model for discharge coefficient prediction of side orifices with different shapes. Flow Measurement and Instrumentation 91: 102372 DOI: 10.1016/j.flowmeasinst.2023.102372

Ding, W., Jia, S., 2023. An Improved Equation for the Bearing Capacity of Concrete-Filled Steel Tube Concrete Short Columns Based on GPR. Buildings 13 (5): 1226 DOI: 10.3390/buildings13051226

Dissanayake, C.K. and Farris, J.A., 2014. Assembly lines of the future: a literature review of research articles from 2000-2014. In Proceedings of the American Society for Engineering Management 2014 International Annual Conference (pp. 1-10).

Dursun, O.F., Kaya, N. and Firat, M., 2012. Estimating discharge coefficient of semi-elliptical side weir using ANFIS. Journal of hydrology, 426, pp.55-62. DOI: https://doi.org/10.1016/j.jhydrol.2012.01.010

Ebtehaj, I., Bonakdari, H., Khoshbin, F., Azimi, H., 2015a. Pareto genetic design of group method of data handling type

neural network for prediction discharge coefficient in rectangular side orifices. Flow Measurement and Instrumentation 41: 67–74 DOI: 10.1016/j.flowmeasinst.2014.10.016

Ebtehaj, I., Bonakdari, H., Zaji, A.H., Azimi, H., Khoshbin, F., 2015b. GMDH-type neural network approach for modeling the discharge coefficient of rectangular sharp-crested side weirs. Engineering Science and Technology, an International Journal 18 (4): 746–757 DOI: 10.1016/j.jestch.2015.04.012

Elshaarawy, M.K., 2025a. Stacked-based hybrid gradient boosting models for estimating seepage from lined canals. Journal of Water Process Engineering 70: 106913 DOI: 10.1016/j.jwpe.2024.106913

Elshaarawy, M.K., 2025b. Metaheuristic-driven CatBoost model for accurate seepage loss prediction in lined canals. Multiscale and Multidisciplinary Modeling, Experiments and Design 8 (5): 235 DOI: 10.1007/s41939-025-00800-8

Elshaarawy, M.K., Armanuos, A.M., 2025a. Simulating the effectiveness of artificial recharge and cutoff walls for saltwater intrusion control with explainable ML and GUI deployment. CATENA 261: 109558 DOI: 10.1016/j.catena.2025.109558

Elshaarawy, M.K., Armanuos, A.M., 2025b. Predicting seawater intrusion wedge length in coastal aquifers using hybrid gradient boosting techniques. Earth Science Informatics 18 (2): 243 DOI: 10.1007/s12145-025-01755-7

Elshaarawy, M.K., Hamed AK. 2024. Stacked Ensemble Model for Optimized Prediction of Triangular Side Orifice Discharge Coefficient. Engineering Optimization DOI: 10.1080/0305215X.2024.2397431

Elshaarawy, M.K., Zeleňáková, M., Armanuos, A.M., 2025. Hydraulic Performance Modeling of Inclined Double Cutoff Walls Beneath Hydraulic Structures Using Optimized Ensemble Machine Learning. Scientific Reports 15 (1): 27592 DOI: 10.1038/s41598-025-10990-3

Eltarabily, M.G., Elshaarawy, M.K., Bali, K.M., Gabr, M.E., 2025. Predicting reference evapotranspiration in semi-arid regions using optimized machine learning models. Journal of Water and Climate Change DOI: 10.2166/wcc.2025.853

Emiroglu, M.E., Agaccioglu, H. and Kaya, N., 2011. Discharging capacity of rectangular side weirs in straight open channels. Flow Measurement and Instrumentation, 22(4), pp.319-330. DOI: https://doi.org/10.1016/j.flowmeasinst.2011.04.003

Emiroglu, M.E., Bilhan, O., Kisi, O., 2011b. Neural networks for estimation of discharge capacity of triangular labyrinth side-weir located on a straight channel. Expert Systems with Applications 38 (1): 867–874 DOI: 10.1016/j.eswa.2010.07.058

Esmailzadeh, M., Heidarpour, M. and Eslamian, S.S., 2015. Flow characteristics of a sharp-crested side sluice gate. Journal of Irrigation and Drainage Engineering, 141(7), p.06014007. DOI: https://doi.org/10.1061/(ASCE)IR.1943-4774.0000852

Gharehbaghi, A., Ghasemlounia, R., Afaridegan, E., Haghiabi, A., Mandala, V., Azamathulla, H.M., Parsaie, A., 2023. A comparison of artificial intelligence approaches in predicting discharge coefficient of streamlined weirs. Journal of Hydroinformatics 25 (4): 1513–1530 DOI: 10.2166/hydro.2023.063

Gharib, R., Heydari, M., Kardar, S., Shabanlou, S., 2020. Simulation of discharge coefficient of side weirs placed on convergent canals using modern self-adaptive extreme learning machine. Applied Water Science 10 (1): 50 DOI: 10.1007/s13201-019-1136-0

Gill, M.A., 1987. Flow Through Side Slots. Journal of Environmental Engineering 113 (5): 1047–1057 DOI: 10.1061/(ASCE)0733-9372(1987)113:5(1047)

Golbraikh, A., Tropsha, A., 2002. Beware of q2! Journal of Molecular Graphics and Modelling 20 (4): 269–276 DOI: 10.1016/S1093-3263(01)00123-1

Hanche-Olsen, H., 2004. Buckingham's pi-theorem. NTNU: http://www. math. ntnu. no/~ hanche/notes/buckingham/buckingham-a4. pdf

Hosny, M., Abdelhaleem, F.S., Elshenhab, A.M., Ibrahim, A., 2025. Prediction of discharge coefficient of submerged gates using a stacking ensemble model. Soft Computing 29 (3): 1911–1929 DOI: 10.1007/s00500-025-10518-x

Hossein Zaji, A., Bonakdari, H., Karimi, S., 2015. Radial Basis Neural Network and Particle Swarm Optimization-based equations for predicting the discharge capacity of triangular labyrinth weirs. Flow Measurement and Instrumentation 45: 341–347 DOI: https://doi.org/10.1016/j.flowmeasinst.2015.08.002

Hussain, A., Ahmad, Z., Asawa, G.L., 2010. Discharge characteristics of sharp-crested circular side orifices in open channels. Flow Measurement and Instrumentation 21 (3): 418–424 DOI: 10.1016/j.flowmeasinst.2010.06.005

Hussain, A., Ahmad, Z., Asawa, G.L., 2011. Flow through sharp-crested rectangular side orifices under free flow condition in open channels. Agricultural Water Management 98 (10): 1536–1544 DOI: https://doi.org/10.1016/j.agwat.2011.05.004

Hussain, A., Ahmad, Z., Ojha, C.S.P., 2014. Analysis of flow through lateral rectangular orifices in open channels. Flow Measurement and Instrumentation 36: 32–35 DOI: 10.1016/j.flowmeasinst.2014.02.002

Hussain, A., Ahmad, Z., Ojha, C.S.P., 2016. Flow through lateral circular orifice under free and submerged flow conditions. Flow Measurement and Instrumentation 52: 57–66 DOI: 10.1016/j.flowmeasinst.2016.09.007

Isleem, H.F., Elshaarawy, M.K., Hamed, A.K., 2024. Analysis of Flow Dynamics and Energy Dissipation in Piano Key and Labyrinth Weirs Using Computational Fluid Dynamics. Computational Fluid Dynamics - Analysis, Simulations, and Applications [Working Title] DOI: 10.5772/intechopen.1006332

Ismael, A.A., Suleiman, S.J., Al-Nima, R.R.O., Al-Ansari, N., 2021. Predicting the discharge coefficient of oblique cylindrical weir using neural network techniques. Arabian Journal of Geosciences 14 (16): 1670 DOI: 10.1007/s12517-021-07911-9

Jamei, M., Ahmadianfar, I., Chu, X. and Yaseen, Z.M., 2021. Estimation of triangular side orifice discharge coefficient under a free flow condition using data-driven models. Flow Measurement and Instrumentation, 77, p.101878. DOI: https://doi.org/10.1016/j.flowmeasinst.2020.101878

Jamei, M., Ahmadianfar, I., Chu, X., Yaseen, Z.M., 2021. Estimation of triangular side orifice discharge coefficient under a free flow condition using data-driven models. Flow Measurement and Instrumentation 77: 101878 DOI: https://doi.org/10.1016/j.flowmeasinst.2020.101878

Jamil, R., Aziz, H.A. and Murshed, M.F., 2023. Water loss prediction model for pipe leaks in water distribution networks laid on sloping terrains. Water Conserv. Manag., 7(2), pp.128-136. DOI: http://doi.org/10.26480/wcm.02.2023.128.136

Karbasi, M., Jamei, M., Ahmadianfar, I., Asadi, A., 2021. Toward the accurate estimation of elliptical side orifice discharge coefficient applying two rigorous kernel-based

data-intelligence paradigms. Scientific Reports 11 (1): 19784 DOI: 10.1038/s41598-021-99166-3

Katlav, M., Ergen, F., 2025. Improved forecasting of the compressive strength of ultra-high-performance concrete (UHPC) via the CatBoost model optimized with different algorithms. Structural Concrete 26 (1): 212–235 DOI: 10.1002/suco.202400163

Khoshbin, F., Bonakdari, H., Ashraf Talesh, S.H., Ebtehaj, I., Zaji, A.H., Azimi, H., 2016. Adaptive neuro-fuzzy inference system multi-objective optimization using the genetic algorithm/singular value decomposition method for modelling the discharge coefficient in rectangular sharp-crested side weirs. Engineering Optimization 48 (6): 933–948 DOI: 10.1080/0305215X.2015.1071807

Khosravinia, P., Nikpour, M.R., Kisi, O., Adnan, R.M., 2023. Predicting Discharge Coefficient of Triangular Side Orifice Using LSSVM Optimized by Gravity Search Algorithm. Water 15 (7): 1341 DOI: 10.3390/w15071341

Luat, N-V., Han, S.W., Lee, K., 2021. Genetic algorithm hybridized with eXtreme gradient boosting to predict axial compressive capacity of CCFST columns. Composite Structures 278: 114733 DOI: https://doi.org/10.1016/j.compstruct.2021.114733

Mahmodian, A.R., Rajabi, A., Izadbakhsh, M.A., Shabanlou, S., 2019. Evaluation of side orifices shape factor using the novel approach self-adaptive extreme learning machine. Modeling Earth Systems and Environment 5 (3): 925–935 DOI: 10.1007/s40808-019-00579-x

Masoud, G., 2003. Flow through Side Sluice Gate. Journal of Irrigation and Drainage Engineering 129 (6): 458–463 DOI: 10.1061/(ASCE)0733-9437(2003)129:6(458)

Megahed, K., Mahmoud, N.S., Abd-Rabou, S.E.M., 2023. Application of machine learning models in the capacity prediction of RCFST columns. Scientific Reports 13 (1): 20878 DOI: 10.1038/s41598-023-48044-1

Moghadam, R.G., Yaghoubi, B., Rajabi, A., Shabanlou, S., Izadbakhsh, M.A., 2022. Evaluation of discharge coefficient of triangular side orifices by using regularized extreme learning machine. Applied Water Science 12 (7): 145 DOI: 10.1007/s13201-022-01665-9

Norouzi, P., Rajabi, A., Izadbakhsh, M.A., Shabanlou, S., Yosefvand, F., Yaghoubi, B., 2020. A new non-tuned self-adaptive machine-learning approach for simulating the discharge coefficient of labyrinth weirs. Irrigation and Drainage 69 (3): 398–416 DOI: https://doi.org/10.1002/ird.2423

Ojha, C.S.P., Subbaiah, D., 1997. Analysis of Flow through Lateral Slot. Journal of Irrigation and Drainage Engineering 123 (5): 402–405 DOI: 10.1061/(ASCE)0733-9437(1997)123:5(402)

Parsaie, A., Azamathulla, H.M., Haghiabi, A.H., 2017a. Prediction of discharge coefficient of cylindrical weir—Gate using GMDH-PSO. ISH J. Hydraul. Eng. 24 DOI: 10.1080/09715010.2017.1372226

Parsaie, A., Haghiabi, A.H., Saneie, M., Torabi, H., 2017b. Predication of discharge coefficient of cylindrical weir-gate using adaptive neuro fuzzy inference systems (ANFIS). Frontiers of Structural and Civil Engineering 11 (1): 111–122 DOI: 10.1007/s11709-016-0354-x

Ramamurthy, A.S., Tim, U.S., Rao, M.V.J., 1987. Weir-Orifice Units for Uniform Flow Distribution. Journal of Environmental Engineering 113 (1): 155–166 DOI: 10.1061/(ASCE)0733-9372(1987)113:1(155)

Ramamurthy, A.S., Tim, U.S., Sarraf, S., 1986a. Rectangular Lateral Orifices in Open Channels. Journal of Environmental Engineering 112 (2): 292–300 DOI: 10.1061/(ASCE)0733-9372(1986)112:2(292)

Ramamurthy, A.S., Tim, U.S., Sarraf, S., 1986b. Rectangular Lateral Orifices in Open Channels. Journal of Environmental Engineering 112 (2): 292–300 DOI: 10.1061/(ASCE)0733-9372(1986)112:2(292)

Razmi, M., Saneie, M., Basirat, S., 2022. Estimating discharge coefficient of side weirs in trapezoidal and rectangular flumes using outlier robust extreme learning machine. Applied Water Science 12 (8): 176 DOI: 10.1007/s13201-022-01698-0

Reza, A., Ahmad, M., Mohammad, R., Izadbakhsh, A., Shabanlou, S., 2019. Evaluation of side orifices shape factor using the novel approach self- adaptive extreme learning machine. Model. Earth Syst. Environ. 5 DOI: 10.1007/s40808-019-00579-x

Saadatnejadgharahassanlou, H., Gharehbaghi, A., Mehdizadeh, S., Kaya, B., Behmanesh, J., 2017. Experimental investigation of discharge coefficient over novel kind of sharp-crested V-notch weir. Flow Measurement and Instrumentation 54: 236–242 DOI: https://doi.org/10.1016/j.flowmeasinst.2017.02.008

Saadatnejadgharahassanlou, H., Zeynali, R.I., Gharehbaghi, A., Mehdizadeh, S., Vaheddoost, B., 2020. Three-dimensional flow simulation over a sharp-crested V-Notch weir. Flow Measurement and Instrumentation 71: 101684 DOI: https://doi.org/10.1016/j.flowmeasinst.2019.101684

Salmasi, F., 2021. Effect of downstream apron elevation and downstream submergence in discharge coefficient of ogee weir. ISH Journal of Hydraulic Engineering 27 (4): 375–384 DOI: 10.1080/09715010.2018.1556125

Seyedian, S.M., Kisi, O., 2024. Uncertainty analysis of discharge coefficient predicted for rectangular side weir using machine learning methods. Journal of Hydrology and Hydromechanics 72 (1): 113–130 DOI: 10.2478/johh-2023-0043

Shang, L., Isleem, H.F., Alsaadawi, M.M., 2025. Deep learning-based modelling of polyvinyl chloride tube-confined concrete columns under different load eccentricities. Engineering Applications of Artificial Intelligence 145: 110217 DOI: 10.1016/j.engappai.2025.110217

Shen, F., Jha, I., Isleem, H.F., Almoghayer, W.J.K., Khishe, M., Elshaarawy, M.K., 2025. Advanced predictive machine and deep learning models for round-ended CFST column. Scientific Reports 15 (1): 6194 DOI: 10.1038/s41598-025-90648-2

Swamee, P.K., Pathak, S.K. and Ali, M.S., 1993. Analysis of rectangular side sluice gate. Journal of irrigation and drainage engineering, 119(6), pp.1026-1035. DOI: https://doi.org/10.1061/(ASCE)0733-9437(1993)119:6(1026)

Swamee, P.K., Pathak, S.K., Mansoor, T., Ojha, C.S.P., 2000. Discharge Characteristics of Skew Sluice Gates. Journal of Irrigation and Drainage Engineering 126 (5): 328–334 DOI: 10.1061/(ASCE)0733-9437(2000)126:5(328)

Theerthagiri, P., 2025. Liver disease classification using histogram-based gradient boosting classification tree with feature selection algorithm. Biomedical Signal Processing and Control 100: 107102 DOI: 10.1016/j.bspc.2024.107102

Vatankhah, A.R., 2016. Discussion of "Stage-Discharge Models for Concrete Orifices: Impact on Estimating Detention Basin Drawdown Time" by W. T. Barlow and D. Brandes. Journal of Irrigation and Drainage Engineering 142 (11): 7016016 DOI: 10.1061/(ASCE)IR.1943-4774.0001102

Vatankhah, A.R., Mirnia, S.H., 2018. Predicting discharge coefficient of triangular side orifice under free flow

conditions. J. Irrig. Drain. Eng. 144 DOI: 10.1061/(ASCE)IR.1943-4774.0001343

Vatankhah, A.R., Rafeifar, F., 2020. Analytical and experimental study of flow through elliptical side orifices. Flow Measurement and Instrumentation 72: 101712 DOI: 10.1016/j.flowmeasinst.2020.101712

Zarei, S., Yosefvand, F., Shabanlou, S., 2020. Discharge coefficient of side weirs on converging channels using extreme learning machine modeling method. Measurement 152 DOI: 10.1016/j.measurement.2019.107321

Zhang, J., Almoghayer, W.J.K., Isleem, H.F,, Negi, B.S., Mahmoud, H.A., Elshaarawy, M.K., 2025. Machine learning for the prediction of the axial load-carrying capacity of FRP reinforced hollow concrete column. Structural Concrete DOI: https://doi.org/10.1002/suco.202400886

Received 10 September 2025
Accepted 25 November 2025